

Pulse Density Modulated ZVS Full-Bridge Converters for Wireless Power Transfer Systems

Hongchang Li, *Member, IEEE*, Kangping Wang, *Member, IEEE*, Jingyang Fang, *Student Member, IEEE*, and Yi Tang, *Senior Member, IEEE*

Abstract—Pulse density modulation (PDM) is an advanced technique for maximum efficiency point tracking (MEPT) of wireless power transfer (WPT) systems. By using PDM, both voltage regulation and efficiency maximization can be achieved without dc/dc converters. PDM is also compatible with the dual-side soft switching technique that utilizes resonant tanks and synchronous rectification. However, this soft switching technique depends on coupling and load conditions. Hard switching may occur when the coupling of coils gets stronger or the equivalent load is not properly controlled. To eliminate the dependence and ensure the soft switching under various operating conditions, this paper proposes a PDM zero-voltage-switching (ZVS) full-bridge converter for WPT systems. The converter employs a ZVS branch between switching nodes to provide a ZVS current, and uses a specially designed modulator to obtain the valid ZVS current waveforms. Experimental results verified the proposed operating principles and showed that the additional power loss caused by the ZVS current is insignificant. The overall efficiency of the WPT prototype was 93 ~ 73 % when the power transfer distance was 0.1 ~ 0.4 m, among which up to 85% efficiency was observed when the distance equaled the coil diameter.

Index Terms—Maximum efficiency point tracking (MEPT), pulse density modulation (PDM), wireless power transfer (WPT), zero voltage switching (ZVS).

I. INTRODUCTION

WIRELESS power transfer (WPT) systems as a special type of power supplies are desired to provide constant output voltage with the maximum efficiency in most applications. However, previous studies showed that both the output voltage (or power) and the efficiency are highly dependent on the system coupling and load conditions [1]. Therefore, maximum efficiency point tracking (MEPT) control strategies were proposed and employed by state-of-the-art WPT systems to track the maximum efficiency while maintaining a constant output voltage against the variations of coupling and load [1-20].

MEPT is based on the fact that a WPT system has a coupling-dependent optimal load for the maximum power transfer

efficiency [21]. The basic idea of MEPT is to convert the system load to the optimal value by a receiving side power converter in real time as per the coupling condition, and simultaneously, control the system input power by a transmitting side power converter to regulate the final output voltage [1]. The roles of the two converters can also be exchanged with proper control algorithms [7, 8, 13].

Regardless of the control algorithms, a WPT system usually requires at least two control degrees of freedom to achieve the two control targets, i.e., the constant output voltage and the maximum efficiency. Conventional MEPT implementations add dc/dc converters on both the transmitting and receiving sides and use the duty ratios of the dc/dc converters as control degrees of freedom, but suffer from the additional power losses and increased system complexity [1]. The phase shift-based MEPT implementations use the phase shift angles of the inverter and the active rectifier as control degrees of freedom, but suffer from the hard switching [3, 8]. The on-off control-based MEPT implementations use low-frequency on-off duty ratios of the inverter and the active rectifier as control degrees of freedom, but suffer from the low average efficiency and large ripples [5, 9, 10]. The recently proposed pulse density modulation (PDM)-based MEPT implementation uses the pulse densities of the inverter and the active rectifier as control degrees of freedom, and eliminates the mentioned disadvantages of other MEPT implementations [15]. However, the soft switching of the PDM WPT system in [15] depends on coupling and load conditions. When the coupling of the coils gets stronger or the equivalent load is not properly controlled, the resonant currents may not be large enough to fully discharge the switch output capacitance, and thus, hard switching may occur, resulting in switching losses, voltage spikes, and noises that may damage the switch. Therefore, the system in [15] cannot operate with a relatively small power transfer distance or a large equivalent load resistance.

To ensure the soft switching of PDM WPT systems under various coupling and load conditions, this paper proposes a PDM zero-voltage-switching (ZVS) full-bridge converter to replace the PDM half-bridge converter in [15]. The proposed

The original conference paper is “A Pulse Density Modulation Method for ZVS Full-Bridge Converters in Wireless Power Transfer Systems”, which will be presented at *IEEE Applied Power Electronics Conference and Exposition (APEC) 2018*. This work was supported by Nanyang Technological University under Grant NTU-SUG M4081608. (*Corresponding author: Yi Tang.*)

Hongchang Li is with the Energy Research Institute, Nanyang Technological University, Singapore (e-mail: hongchangli@ntu.edu.sg).

Kangping Wang is with the School of Electrical Engineering, Xi’an Jiaotong University, Xi’an, China (e-mail: wangkangping@stu.xjtu.edu.cn).

Jingyang Fang and Yi Tang are with the School of Electrical and Electronic Engineering, Nanyang Technological University, Singapore (e-mail: jfang006@e.ntu.edu.sg, yitang@ntu.edu.sg).

converter uses the same soft switching principle as the ZVS class-D converters presented in [22] and [23], i.e., using a ZVS branch to provide the ZVS current. However, the topology of the proposed converter is modified as compared with the ZVS class-D converters: the ZVS branch is connected between the switching nodes rather than in parallel with the lower side switch, and a dc blocking capacitor is inserted on the branch. These modifications make the ZVS branch compatible with PDM. More importantly, a specially designed modulator is proposed to generate the valid pulse sequences so that the ZVS current waveform can be properly shaped and the converter can work stably. The details and experiment will be presented in the following contents.

II. PDM ZVS FULL-BRIDGE CONVERTERS

A. Topology and Principle

Fig. 1 shows the schematic of the main circuit of the proposed PDM ZVS full-bridge converter that operates in inversion mode. The converter is fed by a dc input voltage v_{in} and drives a series resonant tank, whose inductance is L , capacitance is C , and resistance is R . The converter is comprised of a conventional full bridge with switches S_{1-4} and a ZVS branch that consists of a ZVS inductor L_{ZVS} and a dc blocking capacitor C_b . The ZVS branch is connected between the two switching nodes A and B of the two half bridges.

Fig. 2 shows the ideal waveforms when the pulse density d of the converter is 1, where d is defined as the total density of the positive (P) and negative (N) pulses of the switching node voltage u_{AB} . The converter converts v_{in} to P and N of u_{AB} continuously by switching $S_{1,4}$ and $S_{2,3}$ alternately. u_{AB} excites the series resonant tank and results in a resonant current i_L . If the switching frequency f_s equals the resonant frequency f_r , i.e.

$$f_s = f_r = \frac{1}{2\pi\sqrt{LC}} \quad (1)$$

i_L will be in phase with u_{AB} . If C_b is large enough, such that

$$\frac{1}{2\pi\sqrt{L_{ZVS}C_b}} \ll f_s \quad (2)$$

there will be a triangular ZVS current i_{ZVS} that flows on the ZVS branch. i_{ZVS} reaches its peak value at switching time, or more specifically, during dead time T_d . If $T_d \ll 1/f_s$, the absolute peak of i_{ZVS} can be expressed as

$$|i_{ZVS_pk}| = \frac{v_{in}}{4f_s L_{ZVS}}. \quad (3)$$

The integral of i_{ZVS} during T_d is the ZVS charge Q_{ZVS} :

$$Q_{ZVS} = \int_{T_d} i_{ZVS} dt = i_{ZVS_pk} T_d. \quad (4)$$

The ZVS of S_{1-4} can be achieved if Q_{ZVS} is sufficient to discharge the switch output capacitance, i.e.

$$\begin{cases} |Q_{ZVS}| \geq \int_0^{v_{in}} (C_{OSS1} + C_{OSS2}) dv \\ |Q_{ZVS}| \geq \int_0^{v_{in}} (C_{OSS3} + C_{OSS4}) dv \end{cases}. \quad (5)$$

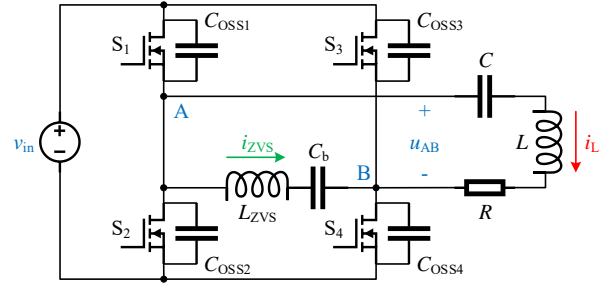


Fig. 1. PDM ZVS full-bridge converter operates in inversion mode.

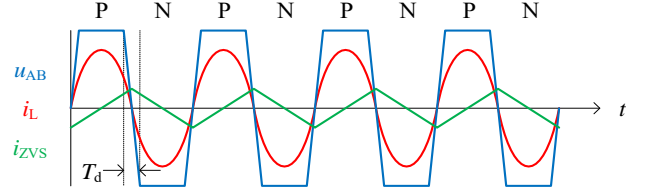


Fig. 2. Ideal waveforms when pulse density d is 1.

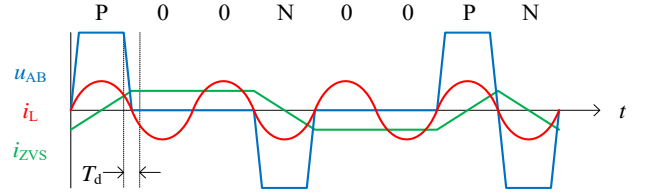


Fig. 3. Ideal waveforms when pulse density d is 0.5.

The range of L_{ZVS} that ensures (5) is derived from (3) and (4), and expressed as

$$L_{ZVS} \leq \frac{T_d}{8f_s C_{OSSQ}} \quad (6)$$

where C_{OSSQ} is the charge equivalent switch output capacitance [22].

Fig. 3 shows the ideal waveforms when d is 0.5. As compared with Fig. 2, some pulses of u_{AB} are removed and the blanks are denoted by “0”. In this case, the ratio of the number of remaining pulses to the total number of P, N and “0” is 0.5. As per the “magnitude-density balance” principle [15], the root-mean-square (RMS) value of the fundamental component of u_{AB} at f_s is

$$U_{AB} = \frac{2\sqrt{2}}{\pi} v_{in} d. \quad (7)$$

Therefore, the magnitude of i_L is lower than that in Fig. 2. On the other hand, the peak value of i_{ZVS} does not change. i_{ZVS} holds its peak during the “0”s so that it is always ready for discharging the switch output capacitance at next switching.

Besides the two cases shown in Fig. 2 and Fig. 3, the converter is able to operate with any specified d within the range of (0, 1] if the sequence of the P, N, and “0” in u_{AB} follows the four rules:

- 1) The total density of P and N equals d ;
- 2) P and N are in phase with i_L ;
- 3) P and N occur alternately;
- 4) P and N are followed by the same number of “0”s.

The 1st and 2nd rules together satisfy the control law of (7). The 2nd rule avoids the back flow of power, which is very inefficient for the power conversion. The 3rd rule prevents i_{ZVS} from continuously increasing or decreasing when it has reached the peak value. The 4th rule ensures the symmetry of i_{ZVS} so that the absolute values of its positive and negative peaks are equal and both sufficient for the ZVS.

B. Modulator

The four rules bring difficulties to the design of the modulator. For example, none of the patterns ‘‘P0N0’’, ‘‘P0’’, and ‘‘PN00’’ is valid for $d = 0.5$ because they violate the 2nd, 3rd, and 4th rules, respectively.

This paper proposes the modulator shown in Fig. 4 to follow the four rules. The modulator has two input signals. One is a clock signal of a frequency f_s that equals the resonant frequency f_r , and the other one is the specified pulse density d . The output signals are u_A^* and u_B^* , which are the references for the switching nodes A and B, respectively. The gate drive signals of $S_{1,4}$ can be generated from u_A^* and u_B^* by using the dead time creators shown in Fig. 5.

The modulator in Fig. 4 operates in two steps. In the first step, a nested frequency modulator ‘‘FM’’ divides the clock frequency by an odd n to generate u_A^* , and a delay unit delays u_A^* for half a clock cycle to generate u_B^* . Fig. 6 shows the waveforms of u_A^* and u_B^* , as well as their difference u_{AB}^* for the cases of $n = 3$ and $n = 1$. It can be verified that u_{AB}^* follows the 2nd, 3rd and 4th rules for any odd n . In the second step, n is determined by delta-sigma modulation to follow the 1st rule. The delta-sigma modulation takes the XOR of u_A^* and u_B^* , which is denoted by u_{XOR} , as the feedback pulses because the pulse density of u_{XOR} equals the total density of the P and N in u_{AB}^* . The difference of d and u_{XOR} is accumulated with a gain k_c by a transfer function block, which is triggered by both the rising and falling edges of the clock signal. The accumulation result is denoted by e . e is sampled by a zero-order holder ‘‘ZoH’’ at the end of each frequency modulation period n/f_s . The sampled e is denoted by e_s . n is derived from e_s by the block ‘‘Calc.’’ in terms of

$$n = 2 \left\lceil \frac{0.5}{\max(e_s, e_{\min})} \right\rceil - 1 \quad (8)$$

where $e_{\min} > 0$ is a lower limit on e_s .

e_{\min} is an important parameter for the modulator. It avoids negative values of n and limits the maximum n :

$$n_{\max} = 2 \left\lceil \frac{0.5}{e_{\min}} \right\rceil - 1 \quad (9)$$

to prevent the frequency modulator ‘‘FM’’ from falling into a too long modulation period. e_{\min} also determines the modulation depth because the minimum achievable d of the modulator is

$$d_{\min} = \frac{1}{n_{\max}}. \quad (10)$$

A smaller e_{\min} gives a larger n_{\max} and enables a deeper modulation. However, the smaller e_{\min} , the smaller k_c is needed to ensure the stability of the delta-sigma modulation, resulting in the slower dynamic response of the modulator. To

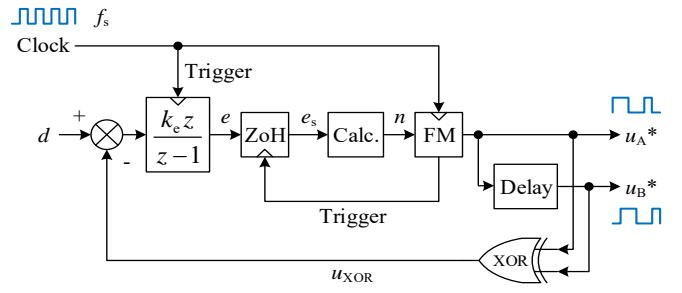


Fig. 4. Schematic of the proposed modulator.

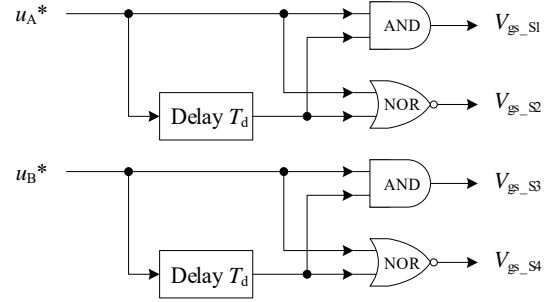


Fig. 5. Dead time creators.

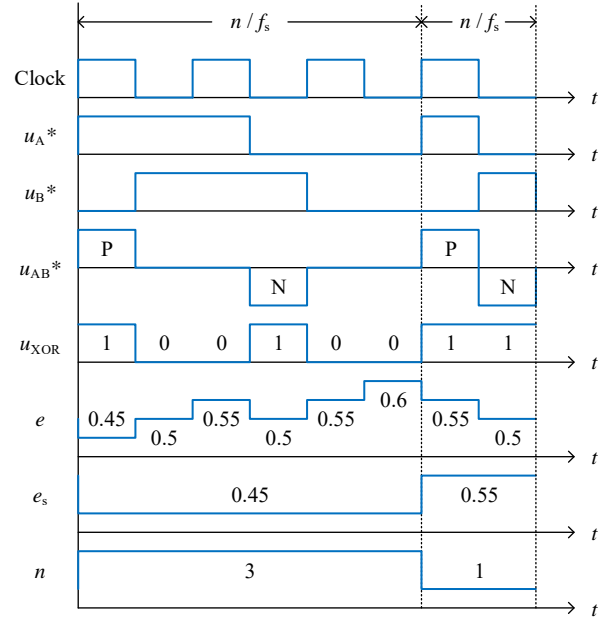


Fig. 6. Ideal waveforms of the proposed modulator when $d = 0.5$.

understand this, considering that for any d within $[d_{\min}, 1]$, there exists an odd n_d , such that

$$\frac{1}{n_d + 2} \leq d \leq \frac{1}{n_d}. \quad (11)$$

The delta-sigma modulation is said to be stable if n is always within $[n_d, n_d + 2]$. As per the modulation logic, this can be ensured if the increase of e during a frequency modulation period $(n_d + 2)/f_s$ is smaller than the resolution of $1/n_d$, and the decrease of e during a frequency modulation period n_d/f_s is smaller than the resolution of $1/(n_d + 2)$, namely

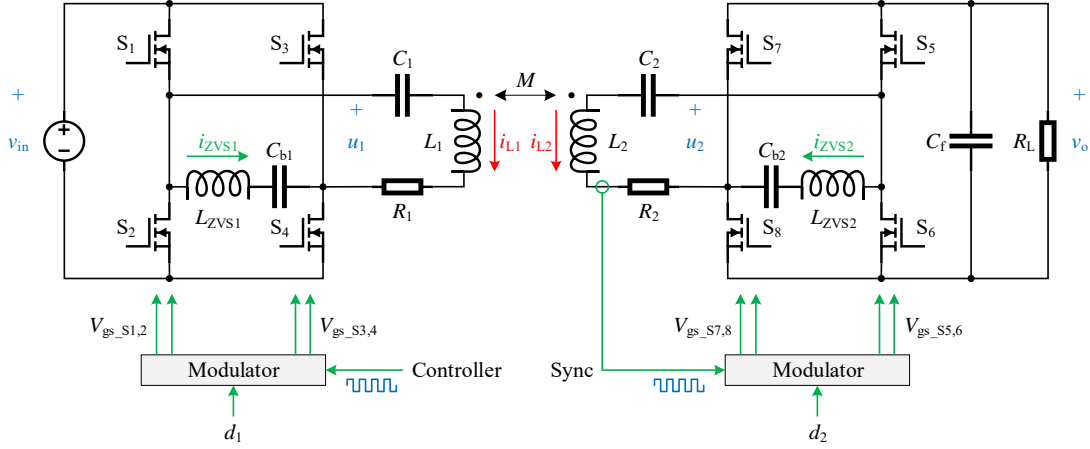


Fig. 7. WPT system employs PDM ZVS full-bridge converters.

$$\begin{cases} |\Delta e_+| = k_c [2(n_d + 2)d - 2] < \frac{1}{n_d - 1} - \frac{1}{n_d + 1} \\ |\Delta e_-| = -k_c [2n_d d - 2] < \frac{1}{n_d + 1} - \frac{1}{n_d + 3} \end{cases} \quad (12)$$

To satisfy (12) for any d within the range of (11), k_c must satisfy

$$k_c < \frac{n_d + 2}{2(n_d + 1)(n_d + 3)}. \quad (13)$$

The worst case of (13) happens when d is close to d_{\min} and $n_d + 2 = n_{\max}$. In this case, (13) can be expressed as

$$k_c < \frac{n_{\max}}{2(n_{\max} - 1)(n_{\max} + 1)}. \quad (14)$$

According to (9) and (14), the smaller e_{\min} , the larger n_{\max} , and consequently, the smaller k_c . Therefore, e_{\min} should be determined by making a tradeoff between the modulation depth and the response speed. A typical value of e_{\min} is 0.2, and correspondingly, $n_{\max} = 5$, $d_{\min} = 0.2$, and $k_c < 0.1042$. In Fig. 6, $k_c = 0.1$ is used as an example.

C. Power Loss Analysis

Although the ZVS branch reduces the switching loss, it increases the conduction loss of the converter from two aspects. First, there is an equivalent series resistance (ESR) R_{ZVS} on the ZVS branch and the average power dissipation on R_{ZVS} during a period T is

$$P_{R_{ZVS}} = \frac{1}{T} \int_0^T i_{ZVS}^2 R_{ZVS} dt. \quad (15)$$

Second, the conduction loss of S_{1-4} increases because the drain currents of S_{1-4} are the sum of i_L and i_{ZVS} when the switch conducts. This increased conduction loss can be expressed as

$$\Delta P_{R_{ds_on}} = \frac{1}{T} \int_0^T 2(i_L + i_{ZVS})^2 R_{ds_on} dt - \frac{1}{T} \int_0^T 2i_L^2 R_{ds_on} dt \quad (16)$$

where R_{ds_on} is the on-state drain-to-source resistance of the switches. Since i_L and i_{ZVS} are orthogonal to each other, (16) can be simplified as

$$\Delta P_{R_{ds_on}} = \frac{1}{T} \int_0^T 2i_{ZVS}^2 R_{ds_on} dt \quad (17)$$

if $T \gg 1/df_s$. The total conduction loss increased by the ZVS current is the sum of (15) and (17), i.e.

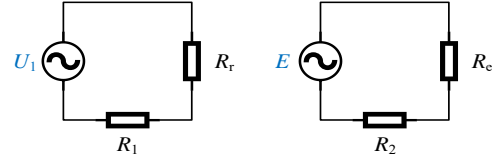


Fig. 8. Ac equivalent circuit.

$$\Delta P_{\text{conduction}} = P_{R_{ZVS}} + \Delta P_{R_{ds_on}} = I_{ZVS}^2 (R_{ZVS} + 2R_{ds_on}) \quad (18)$$

where I_{ZVS} is the RMS value of i_{ZVS} . As per (18), it is better to use the maximum L_{ZVS} given by (6) to minimize I_{ZVS} and $\Delta P_{\text{conduction}}$.

III. THE WPT SYSTEM

Fig. 7 shows a WPT system that employs two PDM ZVS full-bridge converters as the inverter and rectifier. The inverter converts the input dc voltage v_{in} to its switching node voltage u_1 and injects energy into the transmitting side resonator, whose inductance is L_1 , capacitance is C_1 , and ESR is R_1 . The transmitter resonant current is denoted by i_{L1} . Symmetrically, the rectifier converts the output dc voltage v_o to its switching node voltage u_2 and absorbs energy from the receiving side resonator, whose inductance is L_2 , capacitance is C_2 , and ESR is R_2 . The receiver resonant current is denoted by i_{L2} . In addition, the mutual inductance between L_1 and L_2 is M , the filter capacitance is C_f , and the load resistance is R_L .

The transmitting side modulator modulates u_1 using an independent clock signal and a pulse density d_1 . The RMS value of the fundamental component of u_1 is

$$U_1 = \frac{2\sqrt{2}}{\pi} v_{in} d_1. \quad (19)$$

The receiving side modulator modulates u_2 using the pulses synchronized with i_{L2} and a pulse density d_2 . The RMS value of the fundamental component of u_2 is

$$U_2 = \frac{2\sqrt{2}}{\pi} v_o d_2. \quad (20)$$

Thanks to the soft switching nature of the converters, the system can operate under the fully tuned condition, i.e.

$$\omega_s = \frac{1}{\sqrt{L_1 C_1}} = \frac{1}{\sqrt{L_2 C_2}} \quad (21)$$

TABLE I
PARAMETERS OF THE PDM ZVS FULL-BRIDGE CONVERTER

Symbol	Quantity	Value
T_d	Dead time	50 ns
L_{ZVS}	ZVS inductance	10 μ H
C_b	Dc blocking capacitance	1 μ F

where ω_s is the angular frequency of the clock signal. The inverter switching frequency equals $\omega_s/2\pi$ when $d_1 = 1$.

The system steady state behavior can be analyzed using the ac equivalent circuit shown in Fig. 8, where R_e is the ac equivalent load resistance:

$$R_e = \frac{8}{\pi^2} d_2^2 R_L \quad (22)$$

R_r is the reflected resistance:

$$R_r = \frac{(\omega_s M)^2}{R_2 + R_e} \quad (23)$$

and E is the electromotive force induced by i_{L1} . The steady state operating point is given by

$$\begin{cases} I_{L1} = \frac{2\sqrt{2}v_{in}d_1}{\pi(R_1 + R_r)} \\ I_{L2} = \frac{\omega_s M}{R_2 + R_e} I_{L1} \\ v_o = \frac{2\sqrt{2}}{\pi} d_2 I_{L2} R_L \end{cases} \quad (24)$$

where I_{L1} and I_{L2} are the RMS values of i_{L1} and i_{L2} , respectively.

Since the system provides two control degrees of freedom, i.e. d_1 and d_2 , the MEPT control can be adopted by using d_2 to optimize R_e and d_1 to regulate v_o [15].

IV. EXPERIMENT

A. Standalone Operation of the Converter

Fig. 9 shows a prototype of the PDM ZVS full-bridge converter. The prototype was built based on two enhanced-mode gallium nitride half-bridge modules (EPC9003C). An air-core inductor made by Litz wires was used as the ZVS inductor to minimize the ESR. The parameters of the converter are listed in Table I.

The standalone operation was tested by leaving the ac output open circuit under the condition of $v_{in} = 40$ V, $f_s = 1$ MHz, and $d = 0.2 \sim 1$. Fig. 10 shows two of the measured operating waveforms, which are almost the same as the ideal ones, indicating that the ZVS was ideally achieved [23].

The converter power loss, which mainly comes from the conduction loss of the ZVS current, was about 0.2 W for various d , as shown in Fig. 11. Therefore, it can be estimated from (18) that $R_{ZVS} \approx 150$ m Ω , using $I_{ZVS} \approx 1$ A, $R_{ds,on} \approx 25$ m Ω . Another finding from Fig. 11 is that the power loss is not constant but depends on d . This is because both I_{ZVS} and R_{ZVS} vary with d . According to the PDM waveforms, I_{ZVS} increases when d decreases, while R_{ZVS} decreases with d since the ratio of the high frequency ac component in i_{ZVS} decreases.

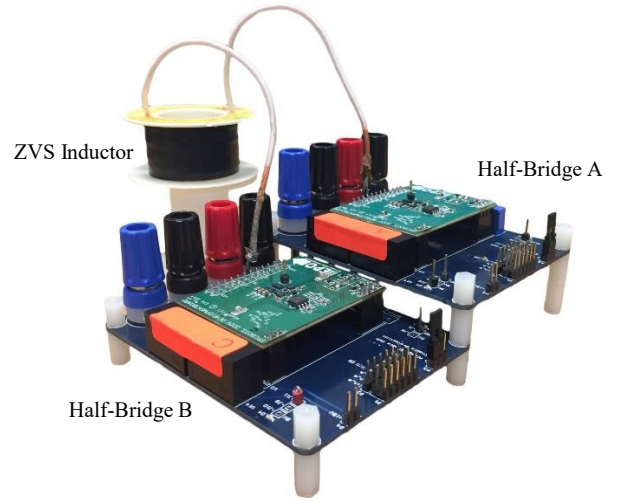


Fig. 9. Prototype PDM ZVS full-bridge converter.

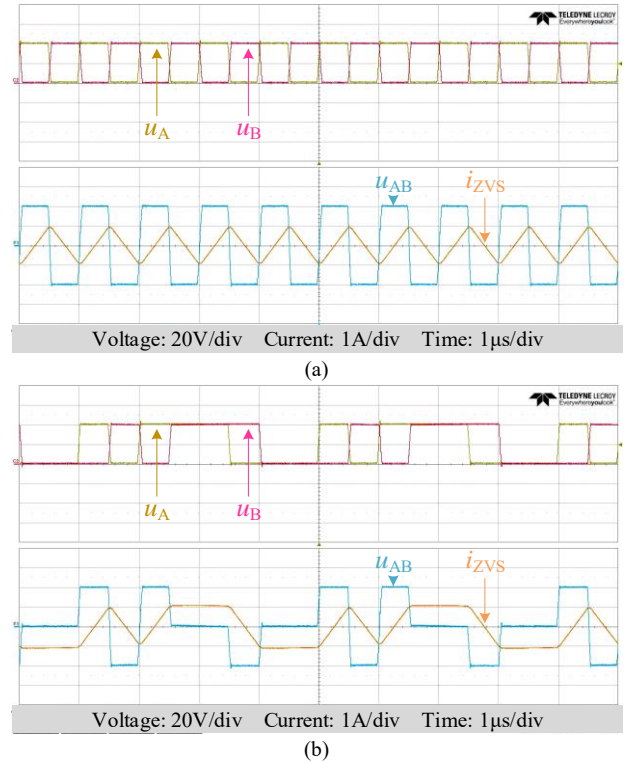


Fig. 10. Operating waveforms of the standalone PDM ZVS full-bridge converter when (a) $d = 1$, and (b) $d = 0.5$.

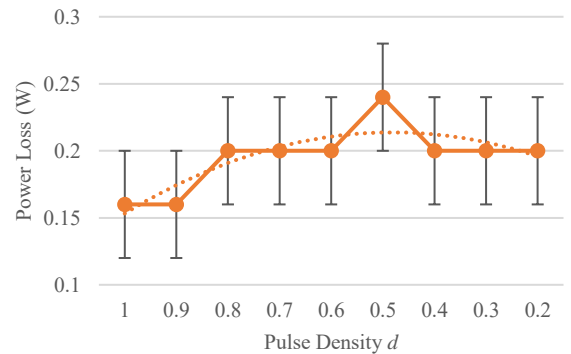


Fig. 11. Power loss at various d .

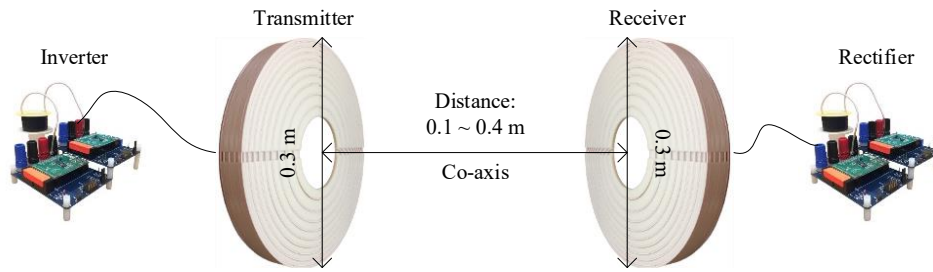


Fig. 12. Spatial configuration of the WPT system.

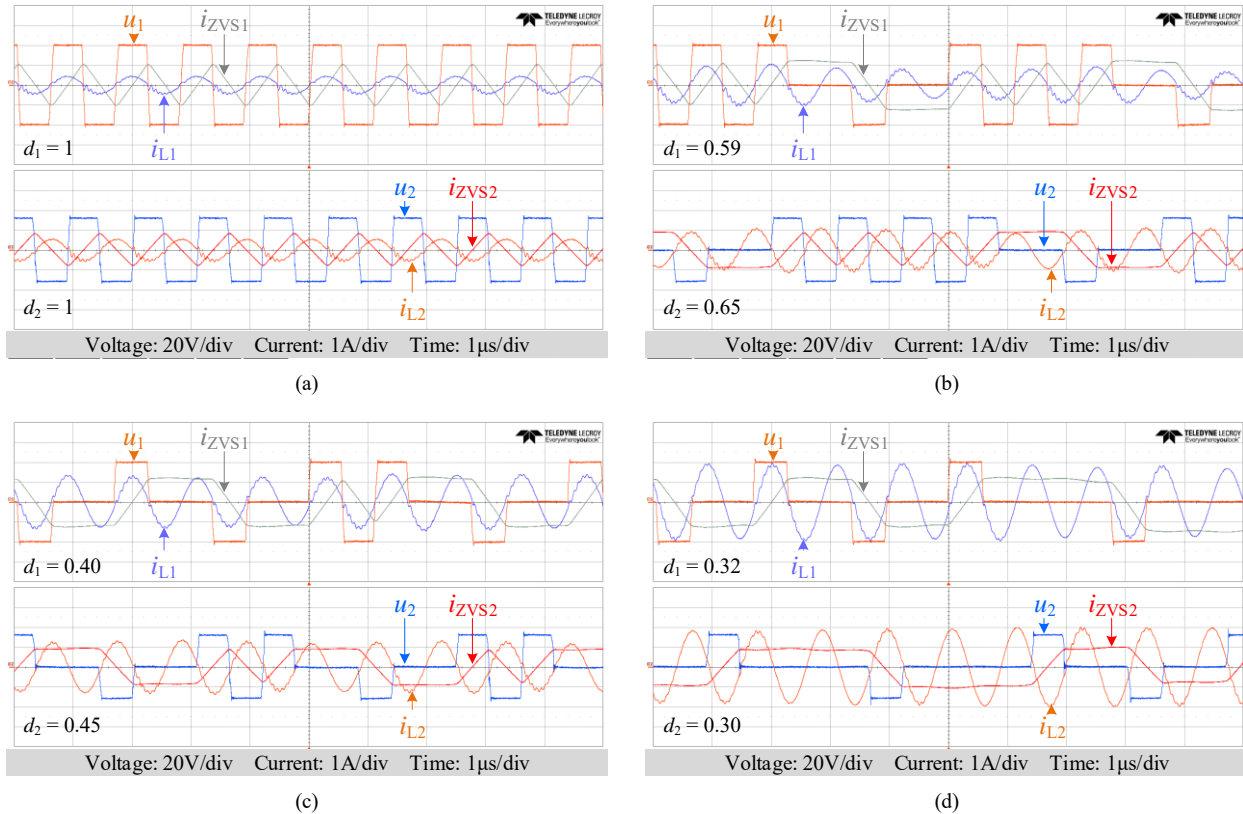


Fig. 13. System operating waveforms when the power transfer distance was (a) 0.1 m, (b) 0.2 m, (c) 0.3 m, and (d) 0.4 m with 100Ω load resistance.

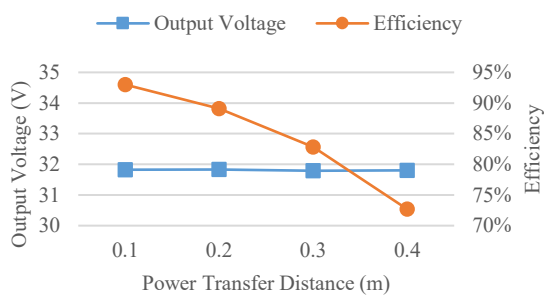


Fig. 14. Effects of voltage regulation and efficiency maximization at various power transfer distances with 100Ω load resistance.

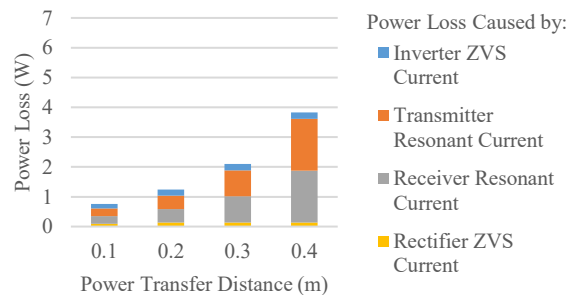


Fig. 15. System loss breakdown at various power transfer distances with 100Ω load resistance.

B. Operating of the WPT System

A WPT system prototype as described in Fig. 7 was built using two PDM ZVS full-bridge converters along with a pair of resonant tanks [15] for the system level verification. The parameters of the system are listed in Table II. The spatial

TABLE II
PARAMETERS OF THE WPT SYSTEM

Symbol	Quantity	Value
$L_{1,2}$	Resonant inductance	76.6 μH
$C_{1,2}$	Resonant capacitance	400 pF
$f_{r1,2}$	Resonant frequency	0.909 MHz
C_f	Filter capacitance	1 μF

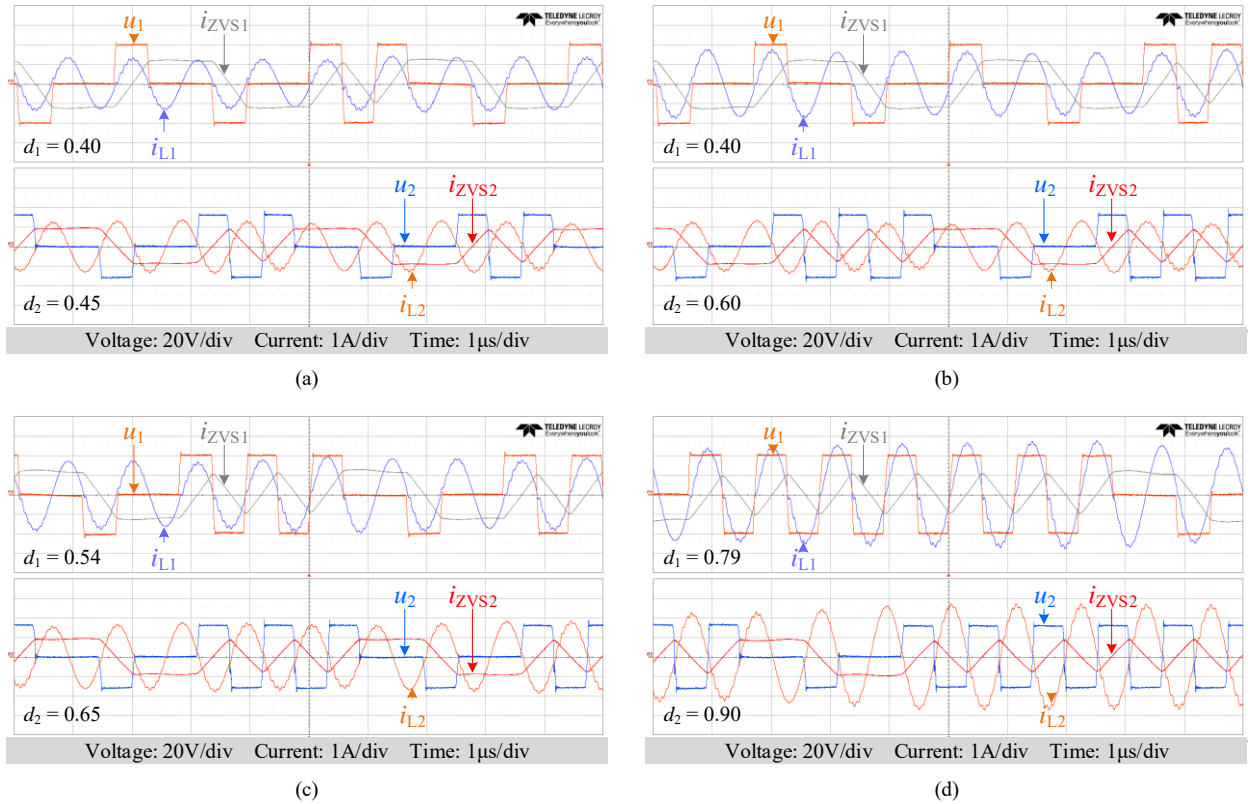


Fig. 16. System operating waveforms when the load resistance was (a) 100 Ω , (b) 75 Ω , (c) 50 Ω , and (d) 25 Ω at 0.3 m power transfer distance.

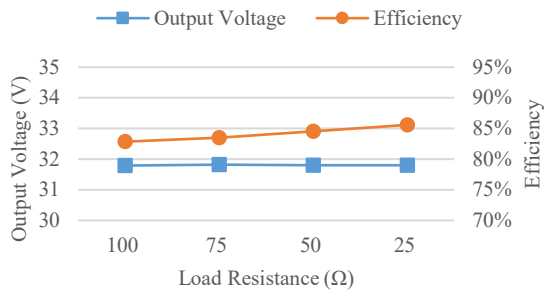


Fig. 17. Effects of voltage regulation and efficiency maximization with various load resistances at 0.3 m power transfer distance.

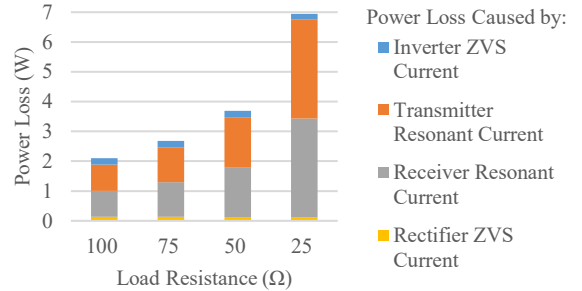


Fig. 18. System loss breakdown with various load resistances at 0.3 m power transfer distance.

configuration is shown in Fig. 12. The input voltage was fixed at 40 V.

The first experiment was carried out at various power transfer distances, 0.1 ~ 0.4 m, with 100 Ω load resistance. The measured operating waveforms are shown in Fig. 13, indicating that the system operated as expected. The MEPT control was manually adopted by adjusting the pulse densities d_1 and d_2 so that the system maintained a constant output voltage, 31.8 V, and achieved the maximum efficiency, 93 ~ 73 %, for various distances, as shown in Fig. 14. The loss breakdown is given by Fig. 15, which includes the losses caused by 1) the inverter ZVS current, 2) the transmitter resonant current, 3) the receiver resonant current, and 4) the rectifier ZVS current. The power losses paid for ZVS are insignificant as compared to the losses caused by the resonant currents, especially at large power transfer distances.

The second experiment was carried out with various load

resistances, 25 ~ 100 Ω , at 0.3 m power transfer distance. The measured operating waveforms, the output voltage and efficiency under MEPT control, and the loss breakdown are shown in Fig. 16, Fig. 17, and Fig. 18, respectively. The system operated as expected with constant output voltage and maximized efficiency. Furthermore, the efficiency increased slightly when the output power became higher because the power losses paid for ZVS did not change with load.

C. Comparison to Reported WPT Systems

Table III compares the WPT prototype in this paper to the representative reported WPT systems with MEPT control. The key parameters, including operating frequency, coil diameter, power transfer distance, coupling coefficient, output power, and overall efficiency are listed in the table. (The overall efficiency considered the power losses on the converters.)

Fig. 19 shows the efficiency with respect to the normalized

TABLE III
REPORTED WPT SYSTEMS WITH MEPT

#	Frequency (MHz)	Coil diameter (mm)	Distance (mm)	Distance (normalized)	Coupling Coefficient	Output power (W)	Efficiency (%)	Reference
1	0.515	270	100	0.37	0.18	25	87	[1]
			150	0.56	0.10		83	
			200	0.74	0.07		79	
			250	0.93	0.04		74	
2	6.780	100	40	0.40	N.A.	10	72	[9]
3	0.592	43	23	0.55	N.A.	5	73	[18]
			28	0.66			66	
			33	0.78			58	
4	0.200	88	25	0.28	0.25	90	89	[13]
			33	0.38	0.17		87	
5	0.098	310	200	0.65	0.07	7	73	[20]
6	0.917	300	500	1.67	0.01	44	70	[15]
7	0.909	300	100	0.33	0.23	10	93	This paper
			200	0.67	0.08		89	
			300	1.00	0.04		83	
			400	1.33	0.02		73	

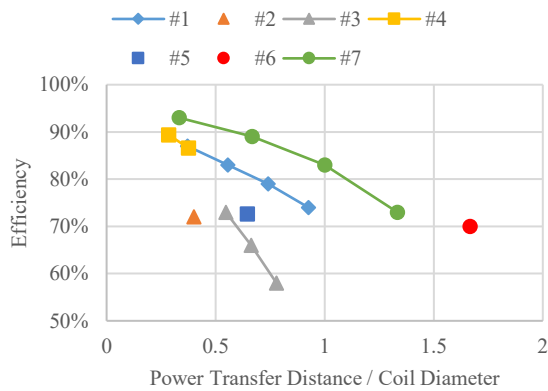


Fig. 19. Efficiency comparison of the WPT systems listed in Table III.

distance, which is defined as power transfer distance over coil diameter. The normalized distance is considered because it is the major limiting factor on the efficiency. It can be seen from Fig. 19 that for any of the WPT systems, the larger normalized distance, the lower efficiency can be achieved, even with MEPT. However, in comparison to other WPT systems, the prototype in this paper achieved higher efficiency at the same normalized distance, and larger normalized distance for the same efficiency.

V. CONCLUSION

This paper proposes a PDM ZVS full-bridge converter along with its modulator. The converter uses the pulse density of switching node voltage as the control degree of freedom for the MEPT control of WPT systems. The converter ensures soft switching regardless of the variations of coupling and load. It also enables the system to operate at the fully tuned condition so that the design and analysis are simplified. Experimental results show that the conduction loss paid for the ZVS is insignificant. Up to 85% overall efficiency can be achieved when the power transfer distance equals the coil diameter. As compared with the reported WPT systems, the prototype in this paper can achieve much higher efficiency in a wide range of power transfer distance. The limitations of the PDM in this paper are the complex modulation logic and the lower limit on pulse density.

REFERENCES

- [1] H. Li, J. Li, K. Wang, W. Chen, and X. Yang, "A maximum efficiency point tracking control scheme for wireless power transfer systems using magnetic resonant coupling," *IEEE Transactions on Power Electronics*, vol. 30, no. 7, pp. 3998-4008, Jul 2015.
- [2] M. Kato, T. Imura, and Y. Hori, "Study on maximize efficiency by secondary side control using dc-dc converter in wireless power transfer via magnetic resonant coupling," *World Electric Vehicle Symposium and Exhibition*, 2013, pp. 1-5.
- [3] T. Diekhans and R. W. De Doncker, "A dual-side controlled inductive power transfer system optimized for large coupling factor variations and partial load," *IEEE Transactions on Power Electronics*, vol. 30, no. 11, pp. 6320-6328, 2015.
- [4] D. Kobayashi, T. Imura, and Y. Hori, "Real-time coupling coefficient estimation and maximum efficiency control on dynamic wireless power transfer for electric vehicles," *IEEE PELS Workshop on Emerging Technologies: Wireless Power*, 2015, pp. 1-6.
- [5] G. Lovison, M. Sato, T. Imura, and Y. Hori, "Secondary-side-only simultaneous power and efficiency control for two converters in wireless power transfer system," *Industrial Electronics Society, IECON 2015 - 41st Annual Conference of the IEEE*, 2015, pp. 4824-4829.
- [6] Y. Narusue, Y. Kawahara, and T. Asami, "Maximum efficiency point tracking by input control for a wireless power transfer system with a switching voltage regulator," *IEEE Wireless Power Transfer Conference*, 2015.
- [7] L. Q. Yuan, B. Y. Li, Y. M. Zhang, F. B. He, K. N. Chen, and Z. M. Zhao, "maximum efficiency point tracking of the wireless power transfer system for the battery charging in electric vehicles," *International Conference on Information Fusion*, 2015, pp. 1101-1107.
- [8] W. X. Zhong and S. Y. R. Hui, "Maximum energy efficiency tracking for wireless power transfer systems," *IEEE Transactions on Power Electronics*, vol. 30, no. 7, pp. 4025-4034, 2015.
- [9] M. Fu, H. Yin, M. Liu, and C. Ma, "Loading and power control for a high-efficiency class-E PA-driven megahertz WPT system," *IEEE Transactions on Industrial Electronics*, vol. 63, no. 11, pp. 6867-6876, 2016.
- [10] K. Hata, T. Imura, and Y. Hori, "Dynamic wireless power transfer system for electric vehicles to simplify ground facilities - power control and efficiency maximization on the secondary side," *IEEE Applied Power Electronics Conference and Exposition*, 2016, pp. 1731-1736.
- [11] X. Dai, X. Li, Y. Li, and P. Hu, "Maximum efficiency tracking for wireless power transfer systems with dynamic coupling coefficient estimation," *IEEE Transactions on Power Electronics*, vol. 33, no. 6, pp. 5005-5015, 2018.
- [12] M. Fu, H. Yin, and C. Ma, "Megahertz multiple-receiver wireless power transfer systems with power flow management and maximum efficiency

point tracking," *IEEE Transactions on Microwave Theory and Techniques*, vol. 65, no. 11, pp. 4285-4293, 2017.

- [13] Z. Huang, S. C. Wong, and C. K. Tse, "Control design for optimizing efficiency in inductive power transfer systems," *IEEE Transactions on Power Electronics*, vol. 33, no. 5, pp. 4523-4534, 2018.
- [14] R. Jin, Z. Yang, and F. Lin, "Mutual inductance identification and maximum efficiency control of wireless power transfer system for the modern tram," *IEEE PELS Workshop on Emerging Technologies: Wireless Power Transfer*, 2017, pp. 70-74.
- [15] H. Li, J. Fang, S. Chen, K. Wang, and Y. Tang, "Pulse density modulation for maximum efficiency point tracking of wireless power transfer systems," *IEEE Transactions on Power Electronics*, vol. 33, no. 6, pp. 5492-5501, 2018.
- [16] H. Li, J. Fang, and Y. Tang, "Delta-sigma modulation for maximum efficiency point tracking of wireless power transfer systems," *IEEE 3rd International Future Energy Electronics Conference and ECCE Asia*, 2017, pp. 434-437.
- [17] R. Mai, Y. Liu, Y. Li, P. Yue, G. Cao, and Z. He, "An active rectifier based maximum efficiency tracking method using an additional measurement coil for wireless power transfer," *IEEE Transactions on Power Electronics*, vol. 33, no. 1, pp. 716-728, 2018.
- [18] X. Tang, J. Zeng, K. P. Pun, S. Mai, C. Zhang, and Z. Wang, "Low-cost maximum efficiency tracking method for wireless power transfer systems," *IEEE Transactions on Power Electronics*, vol. 33, no. 6, pp. 5317-5329, 2018.
- [19] T. D. Yeo, D. Kwon, S. T. Khang, and J. W. Yu, "Design of maximum efficiency tracking control scheme for closed-loop wireless power charging system employing series resonant tank," *IEEE Transactions on Power Electronics*, vol. 32, no. 1, pp. 471-478, 2017.
- [20] W. Zhong and S. Y. R. Hui, "Maximum energy efficiency operation of series-series resonant wireless power transfer systems using on-off keying modulation," *IEEE Transactions on Power Electronics*, vol. 33, no. 4, pp. 3595-3603, 2018.
- [21] A. Kurs, A. Karalis, R. Moffatt, J. D. Joannopoulos, P. Fisher, and M. Soljacic, "Wireless power transfer via strongly coupled magnetic resonances," *Science*, vol. 317, no. 5834, pp. 83-86, 2007.
- [22] M. A. d. Rooij, "The ZVS voltage-mode class-D amplifier, an eGaN FET-enabled topology for highly resonant wireless energy transfer," *IEEE Applied Power Electronics Conference and Exposition*, 2015, pp. 1608-1613.
- [23] M. d. Rooij and Y. Zhang, "eGaN FET based 6.78 MHz differential-mode ZVS class D AirFuel class 4 wireless power amplifier," *International Exhibition and Conference for Power Electronics, Intelligent Motion, Renewable Energy and Energy Management*, 2016, pp. 1-8.



Hongchang Li (S'12-M'16) received the B.Eng. and D.Eng. degrees in electrical engineering from Xi'an Jiaotong University, Xi'an, China, in 2011 and 2016, respectively.

From August 2014 to August 2015, he was a Visiting Scholar with the Molecular Foundry, Lawrence Berkeley National Laboratory, Berkeley, CA, USA. He is currently a Research Fellow with the Energy Research Institute at Nanyang Technological University, Singapore. His research interests include wireless power transfer, electron tomography, and distributed energy storage systems.



Kangping Wang (S'14-M'17) was born in Shaanxi, China, in 1989. He received the B.S. degree in electrical engineering from Xi'an Jiaotong University, Xi'an, China, in 2012. He is currently pursuing the Ph.D. degree in electrical engineering at Xi'an Jiaotong University.

From August 2016 to August 2017, he was with the Department of ePOWER, Electrical and Computer Engineering, Queen's University, Kingston, ON, Canada, as a Visiting Scholar. His research interests include high-frequency power converters and wide bandgap devices.



Jingyang Fang (S'15) received the B.Sc. degree and the M.Sc. degree in electrical engineering from Xi'an Jiaotong University, Xi'an, China, in 2013 and 2015, respectively. He is currently working toward the Ph.D. degree at Nanyang Technological University, Singapore.

His research interests include power quality control, stability analysis and improvement, renewable energy integration, and digital control in more power electronics power systems.

Mr. Fang received the Best Paper Award of Asia Conference on Energy, Power and Transportation Electrification (ACEPT) in 2017.



Yi Tang (S'10-M'14-SM'18) received the B.Eng. degree in electrical engineering from Wuhan University, Wuhan, China, in 2007 and the M.Sc. and Ph.D. degrees in power engineering from the School of Electrical and Electronic Engineering, Nanyang Technological University, Singapore, in 2008 and 2011, respectively.

From 2011 to 2013, he was a Senior Application Engineer with Infineon Technologies Asia Pacific, Singapore. From 2013 to 2015, he was a Postdoctoral Research Fellow with Aalborg University, Aalborg, Denmark. Since March 2015, he has been with Nanyang Technological University, Singapore as an Assistant Professor. He is the Cluster Director of the Advanced Power Electronics Research Program at the Energy Research Institute, Nanyang Technological University.

Dr. Tang was a recipient of the Infineon Top Inventor Award in 2012, the Early Career Teaching Excellence Award in 2017, and four IEEE Prize Paper Awards. He is as an Associate Editor for the IEEE JOURNAL OF EMERGING AND SELECTED TOPICS IN POWER ELECTRONICS.